catalysts

MDPI

Article

Enhanced Photocatalytic Reduction of Cr(VI) by Combined Magnetic TiO_2-Based NFs and Ammonium Oxalate Hole Scavengers

Yin-Hsuan Chang [1] and Ming-Chung Wu [1,2,3,*]

1 Department of Chemical and Materials Engineering, Chang Gung University, Taoyuan 33302, Taiwan; cgu.yinhsuanchang@gmail.com
2 Green Technology Research Center, Chang Gung University, Taoyuan 33302, Taiwan
3 Division of Neonatology, Department of Pediatrics, Chang Gung Memorial Hospital, Linkou, Taoyuan 33305, Taiwan
* Correspondence: mingchungwu@cgu.edu.tw; Tel.: +886-3211-8800 (ext. 3834)

Received: 19 December 2018; Accepted: 5 January 2019; Published: 10 January 2019

Abstract: Heavy metal pollution of wastewater with coexisting organic contaminants has become a serious threat to human survival and development. In particular, hexavalent chromium, which is released into industrial wastewater, is both toxic and carcinogenic. TiO_2 photocatalysts have attracted much attention due to their potential photodegradation and photoreduction abilities. Though TiO_2 demonstrates high photocatalytic performance, it is a difficult material to recycle after the photocatalytic reaction. Considering the secondary pollution caused by the photocatalysts, in this study we prepared $Ag/Fe_3O_4/TiO_2$ nanofibers (NFs) that could be magnetically separated using hydrothermal synthesis, which was considered a benign and effective resolution. For the photocatalytic test, the removal of Cr(VI) was carried out by $Ag/Fe_3O_4/TiO_2$ nanofibers combined with ammonium oxalate (AO). AO acted as a hole scavenger to enhance the electron-hole separation ability, thereby dramatically enhancing the photoreduction efficiency of Cr(VI). The reaction rate constant for $Ag/Fe_3O_4/TiO_2$ NFs in the binary system reached 0.260 min^{-1}, 6.95 times of that of $Ag/Fe_3O_4/TiO_2$ NFs in a single system (0.038 min^{-1}). The optimized $Ag/Fe_3O_4/TiO_2$ NFs exhibited high efficiency and maintained their photoreduction efficiency at 90% with a recyclability of 87% after five cycles. Hence, taking into account the high magnetic separation behavior, $Ag/Fe_3O_4/TiO_2$ NFs with a high recycling capability are a potential photocatalyst for wastewater treatment.

Keywords: TiO_2; magnetic property; photocatalyst; reusable; photoreduction

1. Introduction

With the advancement of various industries comes serious industrial water pollution. Such wastewaters usually contain a complicated mixture of constituents, often involving the co-existence of multiple contaminants such as heavy metals and organic pollutants. With the development of electroplating, metallurgy, leathermaking and more, heavy metal pollution has become a serious threat to human survival and development. One such heavy metals released into industrial wastewater is Cr(VI), which is both toxic and carcinogenic. It has been the first type of carcinogen listed by the World Health Organization's International Cancer Research Institute since 2012. Cr(VI) is easily accumulated in living organisms and can result in vomiting, liver damage, and severe diarrhea. Compared to Cr(VI), trivalent chromium (Cr(III)) is less toxic and more vital for animals and humans [1,2]. The conventional approach for the reduction or removal of Cr(VI) includes electrochemical precipitation [3,4], adsorption [5,6], bacterial reduction [7,8], ion exchange [9,10], photoreduction [11–16], etc. Compared to the above methods, photocatalytic reactions are considered

a clean and promising technology owing to its highly efficient photoreduction of Cr(VI) to the less harmful Cr(III).

TiO_2 is a well-known photocatalyst widely applied for environmental purification due to its advantages, such as its highly active photocatalytic properties, chemical inertness, environmental-friendliness, non-toxicity, and cost-effectiveness [17–24]. It shows great potential in solving the difficult problem of reducing Cr(VI) to Cr(III) in industrial wastewaters. Though TiO_2 demonstrates a high photocatalytic performance, it is difficult to recycle following the photocatalytic reaction. Traditional separation approaches such as filtration and centrifugation have been widely adopted. However, the recycling efficiency is hindered by the loss of photocatalysts. Considering the secondary pollution caused by the photocatalysts, combining TiO_2 with Fe_3O_4 to form magnetic composite materials for the magnetic separation under modest magnetic fields has been seen as a benign and effective resolution [25–28]. To date, there have been many facile methods used to synthesize magnetic iron oxides/TiO_2 hybrid nanomaterial such as sol–gel, metal–organic chemical vapor deposition, the seed-mediated method, and hydrothermal treatment. In spite of introducing magnetic separation by doping Fe_3O_4, the photocatalytic performance could be further enhanced by modifying the shape of Fe_3O_4 to increase the active surface area [29]. In addition, modifying the structure of TiO_2 is also a common method used to enhance photocatalytic performance. Furthermore, combing the ultrafine Fe_3O_4 with one-dimension TiO_2 nanofibers can provide a superior charge transport in a one-dimensional direction, and show high activity.

A great deal of literature has indicated that incorporating Fe_3O_4 into TiO_2 does not improve the photocatalytic properties of TiO_2 as expected [30–32]. The crystallinity of TiO_2 depends on the calcination process, which plays a crucial role in the photocatalytic performance. At the same time, calcination also decreases the saturation magnetization of Fe_3O_4. With the increasing calcination temperature, Fe_3O_4, which has a superparamagnetic phase, would undergo a phase transition to γ-Fe_2O_3 and finally become α-Fe_2O_3, which has a soft ferromagnetic phase [33]. Another problem is the small bandgap of Fe_3O_4, which leads to the fast electron-hole pair recombination in Fe_3O_4/TiO_2 composite material [31]. Therefore, in order to enhance the photocatalytic activity and to maintain the magnetic properties, a lot of research has focused on doping metals to obtain the desired effect [34–38]. In particular, doping Ag into TiO_2 not only enhances the separation of electron-hole pairs, but also maintains the magnetic performance of the Fe_3O_4/TiO_2 composite material. For the Ag-doped TiO_2, the Ag dopants act as the photo-generated electron trapper that enhances the separation of the electron-hole pair and even creates a local electrical field to facilitate electron excitation [39–43].

In this study, in order to achieve both a high photocatalytic activity and a high magnetic property, we prepared Ag and Fe_3O_4 co-doped TiO_2 nanofibers (Ag/Fe_3O_4/TiO_2 NFs) via hydrothermal synthesis followed by a calcination treatment. The Ag/Fe_3O_4/TiO_2 NFs were studied systematically through synchrotron X-ray diffractometer, UV-Vis spectroscopy, field emission scanning electron microscopy (FESEM), and transmission electron microscopy (TEM). For the photocatalytic test, the removal of Cr(VI) was carried out by Ag/Fe_3O_4/TiO_2 NFs combined with ammonium oxalate (AO). Hence, taking into account the high magnetic separation behavior, Ag/Fe_3O_4/TiO_2 NFs with a high recycling capability are a potential photocatalyst for wastewater treatment.

2. Results

Prior to combining magnetic NPs into TiO_2, a basic characterization of Fe_3O_4 was investigated and summarized in Figure 1. The synchrotron X-ray diffractometer was applied to characterize the crystal structure of the Fe_3O_4 NPs as shown in Figure 1a. The characteristic peaks could be indexed to standard Fe_3O_4 (JCPDS No. 019-0629). The method used to determine the bandgap of Fe_3O_4 NPs from the diffusion reflectance is shown schematically in Figure 1b. It was calculated according to $[F(R)hv]^{1/2}$ versus the energy of incident light based on Kubelka–Munk function spectra, $F(R)$. According to Figure 1b, the band gap of Fe_3O_4 NPs was ~0.8 eV. The magnetic property of the Fe_3O_4 NPs were investigated using a (Superconducting quantum interference device magnetometer) SQUID

at 10 K. The magnetic hysteresis loop shown in Figure 1c indicates the ferromagnetic property that exists in Fe_3O_4 NPs. The inset of Figure 1d shows the magnetic separation of Fe_3O_4 NPs from the aqueous dispersion attracted by the Nd-Fe-B magnets. The collected Fe_3O_4 NPs indicated that it could be controlled by an applied magnetic field.

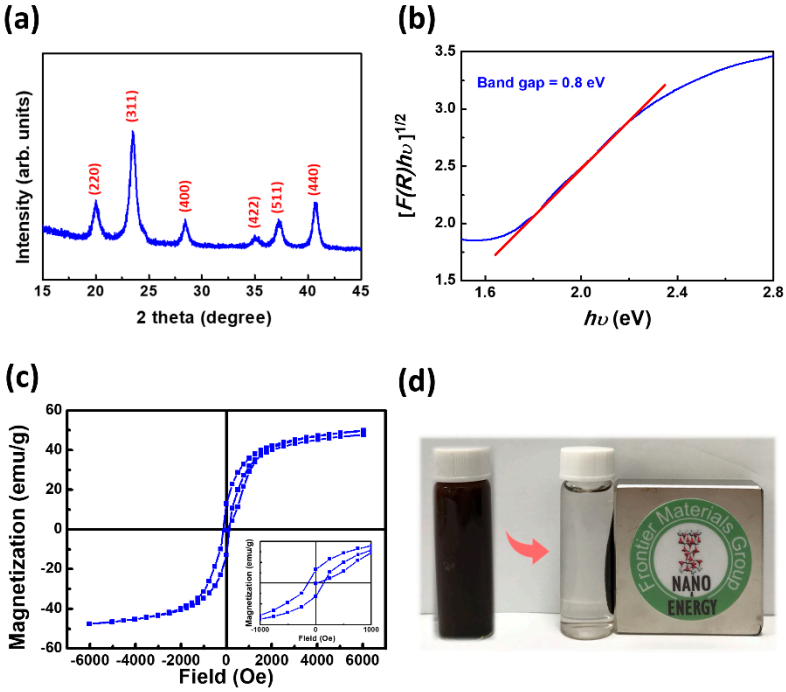

Figure 1. (**a**) Synchrotron X-ray pattern; (**b**) Tauc plot for the indirect band gap; (**c**) magnetic hysteresis loop measured at 10 K of as-synthesized Fe_3O_4 NPs; and (**d**) the Fe_3O_4 suspensions before and after magnetic attraction.

The calcination temperature for the magnetic material is seen as an important factor. For example, as the calcination temperature exceeds 600 °C, it results in a phase transformation from magnetite (Fe_3O_4) to maghemite (γ-Fe_2O_3) to hematite (α-Fe_2O_3) conversions. This phase transformation behavior would cause magnetic material to lose its magnetic properties. In order to maintain the ability to magnetically separate the synthesized TiO_2, the calcination temperature was fixed at 550 °C for the study. Figure 2a shows the synchrotron X-ray patterns Fe_3O_4/TiO_2 with various doping concentrations that depend on the Fe_3O_4/TiO_2 ratio (wt %). The characteristic peaks, which centered at 2θ around 16.71°, 24.27°, 24.81°, 25.31°, 31.33°, 34.99° and 35.71°, could be indexed to anatase phase TiO_2. Pristine TiO_2 exhibited characteristic peaks at 2θ around 18.94°, 19.75° and 22.01° that could be identified as TiO_2 low-temperature phase, β-TiO_2 monoclinic. With the incorporation of Fe_3O_4, the anatase phase TiO_2 became the only phase in the crystal structure, and no characteristic peaks from other phases could be detected. In addition, the radius of an Fe ion (Fe^{2+} ~ 0.76 Å, Fe^{3+} ~ 0.64 Å) is slightly smaller than that of a Ti ion (Ti^{4+} ~ 0.68 Å), indicating that some of doped Fe ion might enter to interstitial voids of TiO_2 lattice [30,44]. The Fe ions in the TiO_2 lattice would act as carrier traps, leading to the electron-hole recombination. Taking into account the recombination phenomenon, the photocatalytic performance could be affected when Fe ions were incorporated into the catalyst. When the doping concentration reached 25.0 wt %, both anatase TiO_2 and Fe_3O_4 peaks were detected. The excessive Fe_3O_4 NPs in the Fe_3O_4-TiO_2 lead to non-uniform doping and to the decrease of the crystallinity of TiO_2. From the magnetic hysteresis loop shown in Figure 2b, as the amount of Fe_3O_4 increased, the magnetization increased as well. In addition, the magnetization was proportional to the doping amount. To optimize the doping concentration, the photocatalytic activity was measured by photoreduction of Cr(VI) in $K_2Cr_2O_7$ aqueous solution under UV-B irradiation.

The photoreduction of Cr(VI) using TiO_2-based catalyst usually follows Langmuir–Hinshelwood kinetics. It can be mathematically simplified to first-order kinetics in the early stage described as $\ln(C_0/C) = kt$, where C_0 is the initial concentration of Cr(VI) in $K_2Cr_2O_7$, C is the remaining Cr(VI) concentration at various times, k is the apparent reaction rate constant, and t is the photodegradation time. The blank experiment was performed under the same conditions but without the existence of the photocatalyst. For the dark experiment, 10.0 wt %-Fe_3O_4/TiO_2 was also tested in dark conditions to observe the adsorption–desorption behavior. From Figure 2c, 10.0 wt %-Fe_3O_4/TiO_2 calcined at 550 °C showed the highest photoreduction performance among other Fe_3O_4/TiO_2 photocatalysts due to the highest crystallinity among the Fe_3O_4/TiO_2 series. High crystallinity can hinder the recombination of photoexcited electrons and holes and thus result in high photocatalytic activity. With further increasing the Fe_3O_4 doping concentration to 15.0 wt % and 25.0 wt %, the excessive dopant might destroy the lattice of TiO_2, thus decreasing the crystallinity of TiO_2 dramatically and form the impurity phases composed of Fe_3O_4, γ-Fe_2O_3 and α-Fe_2O_3. In addition, all of the Fe_3O_4/TiO_2 showed poorer performance compared to the pristine TiO_2, which is in accordance with the XRD spectra. The Fe^{3+} as carrier traps leading to recombination phenomenon and decreased the photocatalytic performance compared with pristine TiO_2.

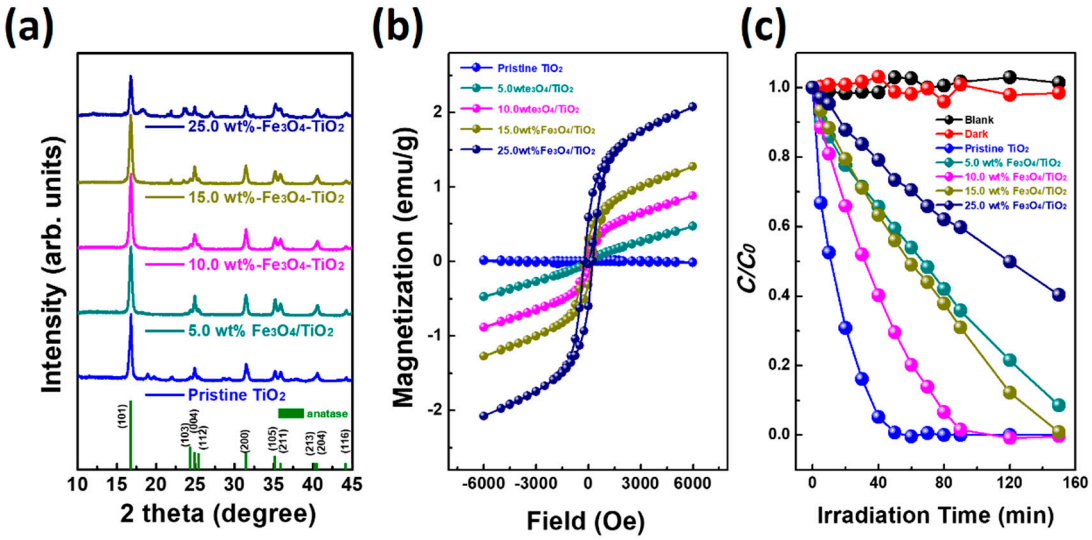

Figure 2. Dependence on the Fe_3O_4/TiO_2 weight ratio (**a**) Synchrotron X-ray patterns; (**b**) magnetic hysteresis loop measured at 10 K; and (**c**) the C/C_o curves for the photoreduction of Cr(VI) in $K_2Cr_2O_7$ aqueous solution under UV-B irradiation using pristine TiO_2 and Fe_3O_4-TiO_2 with various doping concentrations calcined at 550 °C.

Ag was co-doped with 10.0 wt % of Fe_3O_4 into TiO_2 to improve the electron-hole separation further. Figure 3a shows the synchrotron X-ray patterns of the $Ag/Fe_3O_4/TiO_2$ series with various Ag doping concentrations that depended on the amount of Ag (mol %) co-doped with 10 wt % Fe_3O_4/TiO_2. The characteristic peaks of $Ag/Fe_3O_4/TiO_2$ could all be assigned to anatase phase TiO_2 without any Ag signal. The results indicated that the incorporation of Fe_3O_4 and Ag did not destroy the crystal structure of TiO_2. The magnetic hysteresis loop (Figure 3b) illustrates that as the amount of Ag increased, the magnetization decreased. When the excessive Ag dopant was 10.0 mol %, it resulted in a decay of saturation magnetization compared to Fe_3O_4/TiO_2, due to the contribution of the volume of non-magnetic material to the total sample volume. Therefore, the magnetism of the 10.0 mol % $Ag/Fe_3O_4/TiO_2$ was too low for magnetic separation by adding a magnetic field. Figure 3c demonstrates the C/C_o curves for photoreduction of Cr(VI) under UV-B irradiation over the $Ag/Fe_3O_4/TiO_2$ series with different Ag doping concentrations. The blank experiment was also performed under the same conditions but without the presence of the photocatalyst. For the

dark experiment, 5.0 mol % $Ag/Fe_3O_4/TiO_2$ was also tested in dark conditions to eliminate the adsorption–desorption behavior. The 10.0 mol % $Ag/Fe_3O_4/TiO_2$ showed the highest photoreduction performance, even higher than that of pristine TiO_2. Although 10.0 mol % $Ag/Fe_3O_4/TiO_2$ possessed the highest reduction performance, after considering the ability to be magnetically separated, we selected the 5.0 mol % doping level as the optimal photocatalyst. We could also observe that the photoreduction for Ag co-doped with 10 wt % Fe_3O_4/TiO_2 showed the higher performance after the incorporation of Ag compared to 10 wt % Fe_3O_4/TiO_2. This enhancement could be interpreted by the energy level theory, namely that the conduction band of Fe_3O_4 is lower than the conduction band of TiO_2, so the conduction band of TiO_2 becomes an electron capture position. With the further introduction of Ag into Fe_3O_4/TiO_2, Ag could act as another electron trap to enhance the electron-hole separation ability [45].

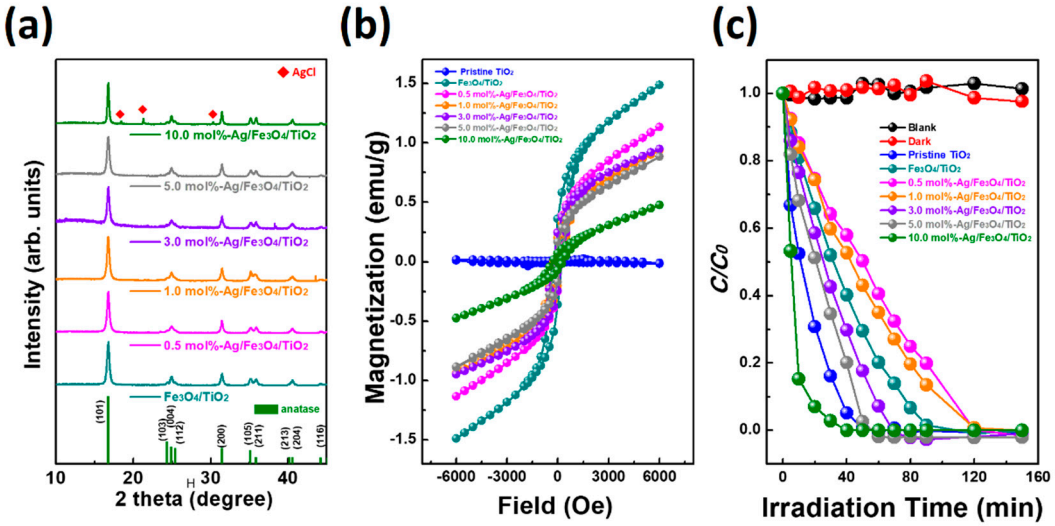

Figure 3. Dependence on the amount of Ag (mol %) co-doped with 10.0 wt % Fe_3O_4/TiO_2. (**a**) Synchrotron X-ray patterns; (**b**) magnetic hysteresis loop measured at 10 K; and (**c**) the C/C_o curves for the photoreduction of Cr(VI) in $K_2Cr_2O_7$ aqueous solution under UV-B irradiation using pristine TiO_2 and $Ag/Fe_3O_4/TiO_2$ with various Ag doping concentration calcined at 550 °C.

After the optimization process, pristine TiO_2, 10.0 wt % Fe_3O_4/TiO_2 (Fe_3O_4/TiO_2) and 5.0 mol % $Ag/Fe_3O_4/TiO_2$ ($Ag/Fe_3O_4/TiO_2$) were compared. The FESEM images of TiO_2-based NFs before and after combining magnetic NPs and Ag are shown in Figure 4. The image shows that the surface of the pristine TiO_2 was very clean and smooth (Figure 4a). When incorporated with Fe_3O_4 NPs, there was no significant morphological change for the Fe_3O_4/TiO_2 (Figure 4b). For $Ag/Fe_3O_4/TiO_2$, the surface became relatively rough and some particles aggregated on it (Figure 4c). On increasing the silver content, the surface charge of TiO_2-based material would gradually decrease. With small amounts of Ag dopant, Ag_2O and AgO might disperse on the surface of TiO_2-based material. When increasing Ag doping concentration, the decrease in surface charge was attributed to an agglomeration of the silver species and a reduction to Ag^0 on the TiO_2 surface [46]. The EDS-characterized elemental compositions and the corresponding results are listed in Table 1. For Fe_3O_4/TiO_2, the ratio of Fe/Ti and Ag/Ti were ~2.9% and ~0.0%, respectively. After incorporating Ag, the ratio of Fe/Ti was ~3.1%, which was approximately the same as Fe_3O_4/TiO_2, and the ratio of Ag/Ti increased to 0.4%. The corresponding ratios of Fe/Ti and Ag/Ti illustrated the existence of Ag in the $Ag/Fe_3O_4/TiO_2$, together with the leading component Ti and Fe. The distinct signals of these elements present in the spectrum confirmed the successful inclusion of Ag ions into the host TiO_2 lattice.

Table 1. The corresponding ratios of Fe/Ti and Ag/Ti for pristine TiO_2, Fe_3O_4/TiO_2 and $Ag/Fe_3O_4/TiO_2$.

Sample	Fe/Ti (%)	Ag/Ti (%)
Pristine TIO_2	0.0	0.0
Fe_3O_4/TiO_2	2.9	0.0
$Ag/Fe_3O_4/TiO_2$	3.1	0.4

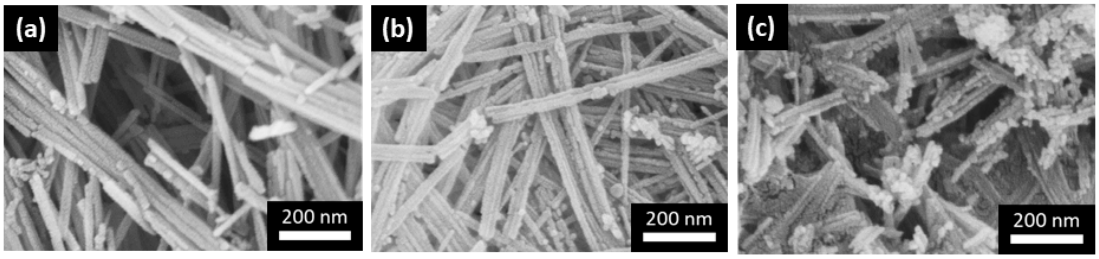

Figure 4. SEM images of (**a**) pristine TiO_2; (**b**) Fe_3O_4/TiO_2 and (**c**) $Ag/Fe_3O_4/TiO_2$.

The Kubelka–Munk function spectra of TiO_2-based materials are shown in Figure 5a. Pristine TiO_2 only showed absorption behavior in the UV range. However, compared to pristine TiO_2, the $F(R)$ spectra of Fe_3O_4/TiO_2 and $Ag/Fe_3O_4/TiO_2$ showed an obvious extension to the visible light region, and the band gap energy also decreased from 3.1 eV to 2.1 eV and 2.0 eV, respectively (Figure 5b). This could be ascribed to the introduction of Fe_3O_4. During the calcination process, the introduced Fe^{3+} could exchange with the lattice position of Ti^{4+} and therefore form an impurity band. Fe_3O_4/TiO_2 and $Ag/Fe_3O_4/TiO_2$ with a decreased forbidden bandwidth could successfully narrow the band gap for the higher absorption behavior in the visible region. This enhanced absorption behavior could generate a lot of photo-excited electrons and holes for photocatalytic reactions.

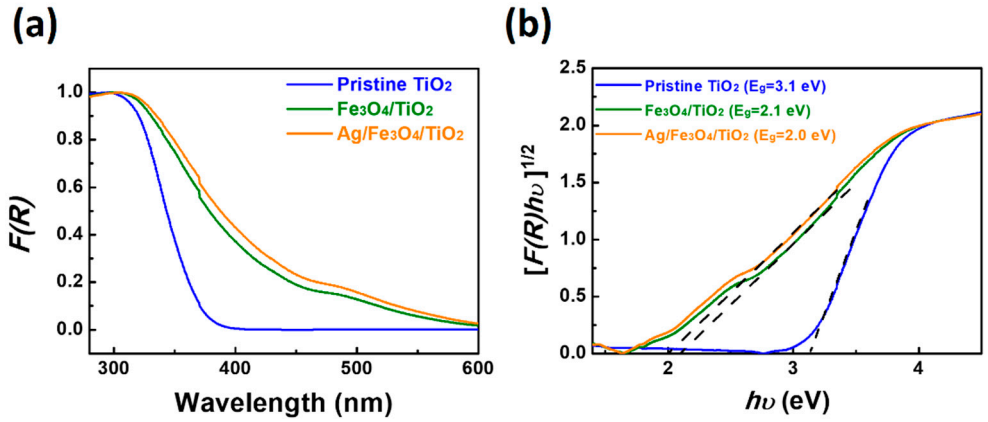

Figure 5. (**a**) Kubelka–Munk function spectra and (**b**) Tauc plot for the indirect band gap of pristine TiO_2, Fe_3O_4/TiO_2 and $Ag/Fe_3O_4/TiO_2$.

The photocatalytic activity test was examined by photoreduction of Cr(VI) to Cr(III). The photoreduction pathways of Cr(VI) on the surface of TiO_2 through UV irradiation can be described by the following reaction sequence (Equations (1)–(6)). After UV light irradiation, photo-excited electron-hole pairs are generated. During the photoreduction reaction of Cr(VI), electrons dominate the entire reaction. Meanwhile, the hole will oxidize H_2O to form the reactive oxygen species OH, which will further react with Cr(III) to generate Cr(VI).

$$TiO_2 + hv \rightarrow h^+ + e^- \quad (1)$$

$$Cr_2O_7^{2-} + 14H^+ + 6e^- \rightarrow 2Cr^{3+} + 7H_2O \quad (2)$$

$$e^- + h^+ \rightarrow recombination \quad (3)$$

$$h^+ + H_2O \rightarrow \cdot OH + H^+ \quad (4)$$

$$h^+ + OH^- \rightarrow \cdot OH \quad (5)$$

$$3 \cdot OH + Cr^{3+} \rightarrow 3OH^- + Cr^{6+} \quad (6)$$

It is unfavorable to reduce Cr(VI) to Cr(III) while Cr(VI) participates in the reaction alone, due to the electron-hole recombination and the oxidation of Cr(III). Figure 6a shows the photoreduction of Cr(VI) over pristine TiO_2, Fe_3O_4/TiO_2 and $Ag/Fe_3O_4/TiO_2$ in a single system for which only Cr(VI) existed in the initial condition. The reduction of Cr(VI) was greatly promoted by the coexistence of ammonium oxalate (AO), and the corresponding results for single systems are also plotted for comparison (Figure 6b). AO is a type of hole scavenger that is widely used for detecting reactive oxygen species during the photocatalytic reaction in order to better understand the reaction mechanism. Therefore, AO would capture the photogenerated holes during the photocatalysis reaction, leaving the photogenerated electrons on the surface of the TiO_2-based NFs. With the help of AO, the separation of the electron-hole was greatly facilitated and thus the reduction performance of Cr(VI) was enhanced. The poor enhancement of pristine TiO_2 compared with Fe_3O_4/TiO_2 and $Ag/Fe_3O_4/TiO_2$ could be due to the bandgap of each sample. A decrease in the bandgap for Fe_3O_4/TiO_2 and $Ag/Fe_3O_4/TiO_2$ resulted in a greater absorption of photons, which was beneficial for the production of electrons and holes required for the photocatalytic reactions. However, the photoexcited electron-hole pair in the Fe_3O_4/TiO_2 and $Ag/Fe_3O_4/TiO_2$ favored a transfer to Fe_3O_4. Holes can provide a faster reaction route with AO, rather than recombining with the electron. Further, the residual electron on the surface of Fe_3O_4/TiO_2 and $Ag/Fe_3O_4/TiO_2$ can reduce Cr(VI) to Cr(III). Therefore, the photoreduction performance for Fe_3O_4/TiO_2 and $Ag/Fe_3O_4/TiO_2$ showed a dramatic enhancement. The reaction rate constant for $Ag/Fe_3O_4/TiO_2$ in binary system achieved 0.260 min^{-1}, which was 6.95 times that of $Ag/Fe_3O_4/TiO_2$ in a single system at 0.038 min^{-1}. These results confirmed the synergetic promotion effect of ammonium oxalate.

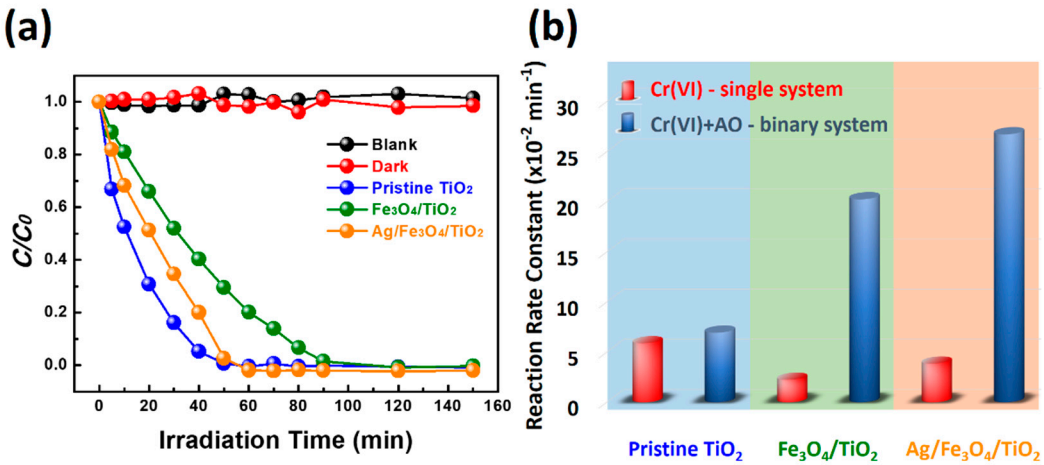

Figure 6. Photocatalytic reaction in (**a**) Cr(VI) single system and (**b**) Cr(VI) + AO binary system with pristine TiO_2, Fe_3O_4/TiO_2, and $Ag/Fe_3O_4/TiO_2$.

The stability and recyclability of the photocatalyst is an important index for practical application. In order to examine the stability and recyclability of $Ag/Fe_3O_4/TiO_2$, the photoreduction of Cr(VI) was repeated five times. Each time, the photocatalysts were recycled by adding a magnetic field. This exhibited a slight decay of reduction efficiency after each cycle, which accounted for the weight loss during every recycle process. After five cycles, the photoreduction efficiency was maintained at 90% (Figure 7a), and the amount of the remaining photocatalyst was 87% (Figure 7b). The stability

and recyclability tests proved that the Cr(VI) photoreduction efficiency over $Ag/Fe_3O_4/TiO_2$ has consistently high stability and recyclability. Therefore, $Ag/Fe_3O_4/TiO_2$ is a potential photocatalyst for wastewater treatment.

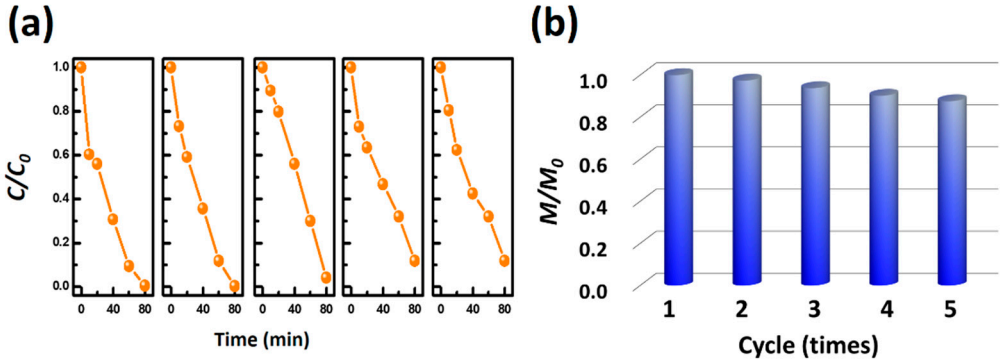

Figure 7. (**a**) Stability and (**b**) recyclability test of $Ag/Fe_3O_4/TiO_2$ for the photocatalytic reduction of Cr(VI) over five cycles.

3. Materials and Methods

3.1. Synthesis of Fe_3O_4 Magnetic NPs

The synthesis of Fe_3O_4 NPs was carried out by the co-precipitation method, in which the iron(II) chloride ($FeCl_2{\cdot}4H_2O$, Acros, 99+%) and iron(III) chloride (($FeCl_3{\cdot}6H_2O$, Acros, 99+%) were used as the raw materials with a molar proportion of 1:2. First, they were dissolved in deionized water and preheated to 60 °C. After that, a 10 M sodium hydroxide aqueous solution (NaOH) acting as a precipitation reagent was added into the mixture solution under continuous stirring for 1 h. The Fe_3O_4 suspension was magnetically separated and washed with deionized water repeatedly until the pH was 7. Finally, the product was air dried at 60 °C.

3.2. Synthesis of $Ag/Fe_3O_4/TiO_2$ NFs

The TiO_2-based NFs were synthesized by hydrothermal method and crystallized by heat treatment. First, 2.5 g anatase phase TiO_2 powder (98%, Sigma-Aldrich, St. Louis, MO, USA), as-synthesized Fe_3O_4 NPs, and silver nitrate ($AgNO_3$, extra pure, Choneye, Taipei, Taiwan) with various stoichiometric ratios were suspended into separate 62.5 mL of 10 M NaOH. The suspension was dispersed uniformly into an ultrasonic bath. After that, the reactants were transferred into a polytetrafluoroethylene-lined autoclave for thermal treatment at 150 °C for 24 h to obtain sodium titanate ($Na_2Ti_3O_7$). Then, various forms of $Na_2Ti_3O_7$ were washed with 0.10 M hydrochloric acid (HCl, 37%, Sigma-Aldrich, St. Louis, MO, USA) to exchange the sodium ion for protons. Finally, the sodium hydrogen titanate ($Na_xH_{2-x}Ti_3O_7$) was filtered and air dried at 80 °C. The dried $Na_xH_{2-x}Ti_3O_7$ was calcined at 550 °C for 12 h at a 5 °C/min heating rate to obtain magnetic TiO_2-based NFs.

3.3. Characterization

To observe the crystal structure, the synchrotron X-ray spectra were collected from 5° to 45° of 2θ with a scan rate of 0.02°/s and a wavelength of ~ 1.025 Å. The Kubelka–Munk function, *F(R)*, spectra were measured and recorded by UV/Vis spectrophotometer (Jacso, V-650, Tokyo, Japan) from 200 to 900 nm wavelength. The magnetic properties of Fe_3O_4 NPs and magnetic TiO_2-based NFs were measured at 10 K temperature using a SQUID magnetometer (MPMS3, Quantum Design, San Diego, CA, USA). The microstructure was characterized by transmission electron microscopy (TEM, spherical-aberration corrected ULTRA-HRTEM, JEM-ARM200FTH, JEOL Ltd., Tokyo, Japan). The morphology and atomic ratio of TiO_2-based NFs were measured by FE-SEM (SU8010, Hitachi, Tokyo, Japan) equipped with EDS (XFlash Detector 5030, Bruker AXS, Karlsruhe, Germany).

3.4. Photocatalytic Measurement

For the measurement of the photoreduction of Cr(VI), 20.0 mg of magnetic TiO_2-based photocatalyst was dispersed into 150.0 mL of potassium dichromate ($K_2Cr_2O_7$, 0.0167 M, Fisher Scientific, CA, USA) with an initial concentration of 1.0 ppm at ambient conditions. As the control group, 20.0 mg of pristine TiO_2 was also dispersed into 150.0 mL $K_2Cr_2O_7$ with an initial concentration of 1.0 ppm at ambient conditions. The two UV-B light lamps (G15T8E, λ_{max} ~312 nm, 8.0 W, Sankyo Denki, Osaka, Japan) were placed ~10.0 cm above the reaction system. Before exposure to light irradiation, the suspensions were put in the dark for 30 min in order to achieve the adsorption equilibrium and thus minimize the surface adsorption behavior. The concentration of retained Cr(VI) was measured by the diphenylcarbazide method. By comparing the intensity of the Cr(VI) characteristic peak located at λ = 540 nm with the calibration curve examined previously, we can obtain its corresponding concentration. In order to examine the mechanism of Cr(VI) photoreduction, 142.2 μL tert-butanol ($(CH_3)_3COH$, ≥99.0%, J.T.Baker, Phillipsburg, NJ, USA) and 24.0 mg ammonium oxalate ($C_2H_8N_2O_4$, 98%, Vetec, trademark of Sigma-Aldrich, St. Louis, MO, USA) were added into $K_2Cr_2O_7$ in the beginning, respectively. The stability and recyclability of the photocatalysts were measured by cycling experiments. After the Cr(VI) photoreduction for each cycle, the magnetic TiO_2 was collected by Nd-Fe-B magnet wrapped with PVC film. After removing the magnetic field, the magnetic TiO_2 was washed three times with ethanol to remove residual ions and molecules and then dried at 80 °C. The fresh 1.0 ppm $K_2Cr_2O_7$ aqueous solution was mixed with the used photocatalyst to perform the second run of photoactivity testing. Similarly, the photocatalyst was recycled to perform the third, fourth, and fifth tests.

4. Conclusions

In this study, we successfully synthesized Ag and Fe_3O_4 co-doped TiO_2 NFs using hydrothermal synthesis followed by thermal treatment in order to achieve high photocatalytic performance and a feasible recycle process. The synthesized $Ag/Fe_3O_4/TiO_2$ exhibited a relatively narrower band gap (2.0 eV) than that of pristine TiO_2 (3.1 eV). For the photoreduction of Cr(VI), electrons dominated the photoreduction efficiency. The photocatalytic process paired with ammonium oxalate could greatly facilitate the separation of electron-hole pairs and thus enhance the reduction rate of Cr(VI). After five cycles of the stability and recyclability test, the photoreduction efficiency was maintained at 90%, and the amount of remaining photocatalyst was maintained at 87%. Consequently, taking into account the high magnetic separation behavior and the high stability, $Ag/Fe_3O_4/TiO_2$ showed great potential to be used for practical wastewater treatment.

Author Contributions: Y.-H.C. performed the research and analyzed the data; Y.-H.C. and M.-C.W. wrote the paper; M.-C.W. was the supervisor and revised the paper. All authors read and approved the final manuscript.

Funding: This research was funded by the Ministry of Science and Technology, Taiwan (MOST 106-2221-E-182-057-MY3 and MSOT 107-2119-M-002-012), Green Technology Research Center, Chang Gung University (QZRPD181) and Chang Gung Memorial Hospital, Linkou (BMRPC74 and CMRPD2H0171).

Acknowledgments: The authors appreciate Wei-Fang Su at National Taiwan University and the Ming-Tao Lee group (TLS BL13A1) at National Synchrotron Radiation Research Center for useful discussion.

Conflicts of Interest: The authors declare no conflict of interest.

References

1. Costa, M. Toxicity and Carcinogenicity of Cr(VI) in Animal Models and Humans. *Crit. Rev. Toxicol.* **1997**, *27*, 431–442. [CrossRef] [PubMed]
2. Rowbotham, A.L.; Levy, L.S.; Shuker, L.K. Chromium in the Environment: An Evaluation of Exposure of the UK General Population and Possible Adverse Health Effects. *J. Toxicol. Environ. Health* **2000**, *3*, 145–178. [CrossRef]

3. Kongsricharoern, N.; Polprasert, C. Electrochemical Precipitation of Chromium (Cr^{6+}) from an Electroplating Wastewater. *Water Res.* **1995**, *31*, 109–117. [CrossRef]
4. Hunsom, M.; Pruksathorn, K.; Damronglerd, S.; Vergnes, H.; Duverneuil, P. Electrochemical Treatment of Heavy Metals (Cu^{2+}, Cr^{6+}, Ni^{2+}) from Industrial Effluent and Modeling of Copper Reduction. *Water Res.* **2005**, *39*, 610–616. [CrossRef] [PubMed]
5. Etemadi, M.; Samadi, S.; Yazd, S.S.; Jafari, P.; Yousefi, N.; Aliabadi, M. Selective Adsorption of Cr(VI) Ions from Aqueous Solutions Using Cr^{6+}-Imprinted Pebax/Chitosan/GO/Aptes Nanofibrous Adsorbent. *Int. J. Biol. Macromol.* **2017**, *95*, 725–733. [CrossRef] [PubMed]
6. Yogeshwaran, V.; Priya, A.K. Removal of Hexavalent Chromium (Cr^{6+}) Using Different Natural Adsorbents—A Review. *J. Chromatogr. Sep. Tech.* **2017**, *8*, 1000392. [CrossRef]
7. Ohtake, H. New Biological Method for Detoxification and Removal of Hexavalent Chromium. *Water Res.* **1992**, *25*, 395–402. [CrossRef]
8. Bennett, R.M.; Cordero, P.R.F.; Bautista, G.S.; Dedeles, G.R. Reduction of Hexavalent Chromium Using Fungi and Bacteria Isolated from Contaminated Soil and Water Samples. *Chem. Ecol.* **2013**, *29*, 320–328. [CrossRef]
9. Xing, Y.; Chen, X.; Wang, D. Electrically Regenerated Ion Exchange for Removal and Recovery of Cr(VI) from Wastewater. *Environ. Sci. Technol.* **2007**, *41*, 1439–1443. [CrossRef]
10. Mekatel, H.; Amokrane, S.; Benturki, A.; Nibou, D. Treatment of Polluted Aqueous Solutions by Ni^{2+}, Pb^{2+}, Zn^{2+}, Cr^{+6},Cd^{+2} and Co^{+2} Ions by Ion Exchange Process Using Faujasite Zeolite. *Procedia Eng.* **2012**, *33*, 52–57. [CrossRef]
11. Cai, J.; Wu, X.; Zheng, F.; Li, S.; Wu, Y.; Lin, Y.; Lin, L.; Liu, B.; Chen, Q.; Lin, L. Influence of TiO_2 Hollow Sphere Size on Its Photo-Reduction Activity for Toxic Cr(VI) Removal. *J. Colloid Interface Sci.* **2017**, *490*, 37–45. [CrossRef] [PubMed]
12. Lu, D.; Yang, M.; Fang, P.; Li, C.; Jiang, L. Enhanced Photocatalytic Degradation of Aqueous Phenol and Cr(VI) over Visible-Light-Driven Tbxoy Loaded TiO_2-Oriented Nanosheets. *Appl. Surf. Sci.* **2017**, *399*, 167–184. [CrossRef]
13. Wang, L.; Zhang, C.; Gao, F.; Mailhot, G.; Pan, G. Algae Decorated TiO_2/Ag Hybrid Nanofiber Membrane with Enhanced Photocatalytic Activity for Cr(VI) Removal under Visible Light. *Chem. Eng. J.* **2017**, *314*, 622–630. [CrossRef]
14. Li, Y.; Liu, Z.; Wu, Y.; Chen, J.; Zhao, J.; Jin, F.; Na, P. Carbon Dots-TiO_2 Nanosheets Composites for Photoreduction of Cr(VI) under Sunlight Illumination: Favorable Role of Carbon Dots. *Appl. Catal. B* **2018**, *224*, 508–517. [CrossRef]
15. Wang, W.; Lai, M.; Fang, J.; Lu, C. Au and Pt Selectively Deposited on {001}-Faceted TiO_2 toward SPR Enhanced Photocatalytic Cr(VI) Reduction: The Influence of Excitation Wavelength. *Appl. Surf. Sci.* **2018**, *439*, 430–438. [CrossRef]
16. Ngo, A.; Nguyen, H.; Hollmann, D. Criticial Assessment of the Photocatalytic Reduction of Cr(VI) over Au/TiO_2. *Catalysts* **2018**, *8*, 606. [CrossRef]
17. Tan, L.-L.; Ong, W.-J.; Chai, S.-P.; Mohamed, A.R. Visible-Light-Activated Oxygen-Rich TiO_2 as Next Generation Photocatalyst: Importance of Annealing Temperature on the Photoactivity toward Reduction of Carbon Dioxide. *Chem. Eng. J.* **2016**, *283*, 1254–1263. [CrossRef]
18. Busiakiewicz, A.; Kisielewska, A.; Piwoński, I.; Batory, D. The Effect of Fe Segregation on the Photocatalytic Growth of Ag Nanoparticles on Rutile TiO_2 (001). *Appl. Surf. Sci.* **2017**, *401*, 378–384. [CrossRef]
19. Low, J.; Cheng, B.; Yu, J. Surface Modification and Enhanced Photocatalytic CO_2 Reduction Performance of TiO_2: A Review. *Appl. Surf. Sci.* **2017**, *392*, 658–686. [CrossRef]
20. Tan, L.-L.; Ong, W.-J.; Chai, S.-P.; Mohamed, A.R. Photocatalytic Reduction of CO_2 with H_2O over Graphene Oxide-Supported Oxygen-Rich TiO_2 Hybrid Photocatalyst under Visible Light Irradiation: Process and Kinetic Studies. *Chem. Eng. J.* **2017**, *308*, 248–255. [CrossRef]
21. Zhang, Y.; Gu, D.; Zhu, L.; Wang, B. Highly Ordered Fe^{3+}/TiO_2 Nanotube Arrays for Efficient Photocataltyic Degradation of Nitrobenzene. *Appl. Surf. Sci.* **2017**, *420*, 896–904. [CrossRef]
22. Duan, Y.; Liang, L.; Lv, K.; Li, Q.; Li, M. TiO_2 Faceted Nanocrystals on the Nanofibers: Homojunction TiO_2 Based Z-Scheme Photocatalyst for Air Purification. *Appl. Surf. Sci.* **2018**, *456*, 817–826. [CrossRef]
23. Makal, P.; Das, D. Self-Doped TiO_2 Nanowires in TiO_2-B Single Phase, TiO_2-B/Anatase and TiO_2-Anatase/Rutile Heterojunctions Demonstrating Individual Superiority in Photocatalytic Activity under Visible and UV Light. *Appl. Surf. Sci.* **2018**, *455*, 1106–1115. [CrossRef]
24. Wu, M.-C.; Hsiao, K.-C.; Chang, Y.-H.; Chan, S.-H. Photocatalytic Hydrogen Evolution of Palladium Nanoparticles Decorated Black TiO_2 Calcined in Argon Atmosphere. *Appl. Surf. Sci.* **2018**, *430*, 407–414. [CrossRef]

25. Jing, J.; Li, J.; Feng, J.; Li, W.; Yu, W.W. Photodegradation of Quinoline in Water over Magnetically Separable Fe_3O_4/TiO_2 Composite Photocatalysts. *Chem. Eng. J.* **2013**, *219*, 355–360. [CrossRef]
26. Li, Z.-J.; Huang, Z.-W.; Guo, W.-L.; Wang, L.; Zheng, L.-R.; Chai, Z.-F.; Shi, W.-Q. Enhanced Photocatalytic Removal of Uranium(VI) from Aqueous Solution by Magnetic TiO_2/Fe_3O_4 and Its Graphene Composite. *Environ. Sci. Technol.* **2017**, *51*, 5666–5674. [CrossRef] [PubMed]
27. Yu, Y.; Yan, L.; Cheng, J.; Jing, C. Mechanistic Insights into TiO_2 Thickness in Fe_3O_4@TiO_2-GO Composites for Enrofloxacin Photodegradation. *Chem. Eng. J.* **2017**, *325*, 647–654. [CrossRef]
28. Liu, M.-C.; Liu, B.; Sun, X.-Y.; Lin, H.-C.; Lu, J.-Z.; Jin, S.-F.; Yan, S.-Q.; Li, Y.-Y.; Zhao, P. Core/Shell Structured Fe_3O_4@TiO_2-DNM Nanospheres as Multifunctional Anticancer Platform: Chemotherapy and Photodynamic Therapy Research. *J. Nanosci. Nanotechnol.* **2018**, *18*, 4445–4456. [CrossRef] [PubMed]
29. Wu, W.; Xiao, X.; Zhang, S.; Ren, F.; Jiang, C. Facile Method to Synthesize Magnetic Iron Oxides/TiO_2 Hybrid Nanoparticles and Their Photodegradation Application of Methylene Blue. *Nanoscale Res. Lett.* **2011**, *6*, 533. [CrossRef]
30. Shojaei, A.F.; Shams-Nateri, A.; Ghomashpasand, M. Magnetically Recyclable Fe^{3+}/TiO_2@Fe_3O_4Nanocomposites Towards Degradation of Direct Blue 71 under Visible-Light Irradiation. *IET Micro Nano Lett.* **2017**, *12*, 161–165. [CrossRef]
31. Jia, X.; Dai, R.; Lian, D.; Han, S.; Wu, X.; Song, H. Facile Synthesis and Enhanced Magnetic, Photocatalytic Properties of One-Dimensional Ag@Fe_3O_4-TiO_2. *Appl. Surf. Sci.* **2017**, *392*, 268–276. [CrossRef]
32. Wang, H.; Fei, X.; Wang, L.; Li, Y.; Xu, S.; Sun, M.; Sun, L.; Zhang, C.; Li, Y.; Yang, Q.; et al. Magnetically Separable Iron Oxide Nanostructures-TiO_2 Nanofibers Hierarchical Heterostructures: Controlled Fabrication and Photocatalytic Activity. *New J. Chem.* **2011**, *35*, 1795–1802. [CrossRef]
33. Jafari, A.; Shayesteh, S.F.; Salouti, M.; Boustani, K. Effect of Annealing Temperature on Magnetic Phase Transition in Fe_3O_4 Nanoparticles. *J. Magn. Magn. Mater.* **2015**, *379*, 305–312. [CrossRef]
34. Wang, W.-K.; Chen, J.-J.; Gao, M.; Huang, Y.-X.; Zhang, X.; Yu, H.-Q. Photocatalytic Degradation of Atrazine by Boron-Doped TiO_2 with a Tunable Rutile/Anatase Ratio. *Appl. Catal. B* **2016**, *195*, 69–76. [CrossRef]
35. Rossi, G.; Pasquini, L.; Catone, D.; Piccioni, A.; Patelli, N.; Paladini, A.; Molinari, A.; Caramori, S.; O'Keeffe, P.; Boscherini, F. Charge Carrier Dynamics and Visible Light Photocatalysis in Vanadium-Doped TiO_2 Nanoparticles. *Appl. Catal. B* **2018**, *237*, 603–612. [CrossRef]
36. Wu, M.-C.; Wu, P.-Y.; Lin, T.-H.; Lin, T.-F. Photocatalytic Performance of Cu-Doped TiO_2 Nanofibers Treated by the Hydrothermal Synthesis and Air-Thermal Treatment. *Appl. Surf. Sci.* **2018**, *430*, 390–398. [CrossRef]
37. Avilés-García, O.; Espino-Valencia, J.; Romero-Romero, R.; Rico-Cerda, J.; Arroyo-Albiter, M.; Solís-Casados, D.; Natividad-Rangel, R. Enhanced Photocatalytic Activity of Titania by Co-Doping with Mo and W. *Catalysts* **2018**, *8*, 631. [CrossRef]
38. Ramírez-Sánchez, I.; Bandala, E. Photocatalytic Degradation of Estriol Using Iron-Doped TiO_2 under High and Low UV Irradiation. *Catalysts* **2018**, *8*, 625. [CrossRef]
39. Ali, T.; Ahmed, A.; Alam, U.; Uddin, I.; Tripathi, P.; Muneer, M. Enhanced Photocatalytic and Antibacterial Activities of Ag-Doped TiO_2 Nanoparticles under Visible Light. *Mater. Chem. Phys* **2018**, *212*, 325–335. [CrossRef]
40. Mandari, K.K.; Do, J.Y.; Police, A.K.R.; Kang, M. Natural Solar Light-Driven Preparation of Plasmonic Resonance-Based Alloy and Core-Shell Catalyst for Sustainable Enhanced Hydrogen Production: Green Approach and Characterization. *Appl. Catal. B* **2018**, *231*, 137–150. [CrossRef]
41. Chen, S.-H.; Chan, S.-H.; Lin, Y.-T.; Wu, M.-C. Enhanced Power Conversion Efficiency of Perovskite Solar Cells Based on Mesoscopic Ag-Doped TiO_2 Electron Transport Layer. *Appl. Surf. Sci.* **2019**, *469*, 18–26. [CrossRef]
42. Wu, M.-C.; Liao, Y.-H.; Chan, S.-H.; Lu, C.-F.; Su, W.-F. Enhancing Organolead Halide Perovskite Solar Cells Performance through Interfacial Engineering Using Ag-Doped TiO_2 Hole Blocking Layer. *Sol. RRL* **2018**, *2*, 1800072. [CrossRef]
43. Akel, S.; Dillert, R.; Balayeva, N.; Boughaled, R.; Koch, J.; El Azzouzi, M.; Bahnemann, D. Ag/Ag_2O as a Co-Catalyst in TiO_2 Photocatalysis: Effect of the Co-Catalyst/Photocatalyst Mass Ratio. *Catalysts* **2018**, *8*, 647. [CrossRef]
44. Wen, L.; Liu, B.; Zhao, X.; Nakata, K.; Murakami, T.; Fujishima, A. Synthesis, Characterization, and Photocatalysis of Fe-Doped TiO_2: A Combined Experimental and Theoretical Study. *Int. J. Photoenergy* **2012**, *2012*, 368750. [CrossRef]

45. Zhan, J.; Zhang, H.; Zhu, G. Magnetic Photocatalysts of Cenospheres Coated with Fe_3O_4/TiO_2 Core/Shell Nanoparticles Decorated with Ag Nanopartilces. *Ceram. Int.* **2014**, *40*, 8547–8559. [CrossRef]
46. Mogal, S.; Gandhi, V.G.; Mishra, M.; Tripathi, S.; Shripathi, T.; Joshi, P.; Shah, D. Single-Step Synthesis of Silver-Doped Titanium Dioxide: Influence of Silver on Structural, Textural, and Photocatalytic Properties. *Ind. Eng. Chem. Res.* **2014**, *53*, 5749–5758. [CrossRef]